Research Square

Preprints are preliminary reports that have not undergone peer review.
They should not be considered conclusive, used to inform clinical practice,
or referenced by the media as validated information.

Indirect Thrust Measurement of the MP2S Pulsed Magnetoplasmadynamic Thruster

Rune Fritzsche

fritzscher@irs.uni-stuttgart.de

University of Stuttgart

Felix Schäfer

University of Stuttgart

Georg Herdrich

University of Stuttgart

Thomas Yung

COMAT

Julien Scheiner

COMAT

Grégoire Brivary-Couret

COMAT

Luc Herrero

COMAT

Research Article

Keywords: Pulsed thruster, Magnetoplasmadynamics, Thrust determination

Posted Date: April 9th, 2026

DOI: https://doi.org/10.21203/rs.3.rs-9245821/v1

License: This work is licensed under a Creative Commons Attribution 4.0 International License.
Read Full License

Additional Declarations: No competing interests reported.

Indirect Thrust Measurement of the MP^{2}S Pulsed Magnetoplasmadynamic Thruster

Rune Fritzsche[1*], Felix Schäfer[1], Georg Herdrich[1], Thomas Yung[2†], Julien Scheiner[2†], Grégoire Brivary-Couret[2†], Luc Herrero[2†]

[1*]Institute of Space Systems, University of Stuttgart, Pfaffenwaldring 29, Stuttgart, 70569, Baden-Württemberg, Germany.
[2]COMAT, 6 Chem. de Vignalis, Flourens, 31130, Haute-Garonne, France.

*Corresponding author(s). E-mail(s): fritzscher@irs.uni-stuttgart.de;
Contributing authors: fschaefer@irs.uni-stuttgart.de; herdrich@irs.uni-stuttgart.de; t.yung@comat.space; j.scheiner@comat.space; g.brivary-couret@comat.space; l.herrero@comat.space;
†These authors contributed equally to this work.

Abstract

Pulsed, gas-fed electric propulsion systems are a promising option for future small satellite missions but pose significant challenges for accurate thrust characterization due to parasitic forces introduced by propellant feed lines. This paper presents and experimentally demonstrates an indirect thrust measurement methodology for a pulsed quasi steady-state magnetoplasmadynamic thruster prototype of the Modular Pulsed Propulsion System (MP^{2}S MPDT). The thruster plume is directed onto a graphite target mounted on a high-precision thrust balance, decoupling the balance mechanically from the gas supply system. Since the impulse transfer between the argon plume and the target is unknown, it is quantified using LAMMPS molecular dynamics simulations to obtain an impulse transfer correction factor. The impulse bit is measured using nanometer-resolution pendulum displacement measurements processed via sinusoidal curve fitting and wavelet filtering. A comprehensive uncertainty analysis based on Gaussian error propagation is performed, accounting for calibration, sensor resolution, geometry, timing, frequency determination, damping, and impulse transfer. The methodology is used to determine impulse bit, specific impulse, and thrust efficiency of the MP^{2}S MPDT, demonstrating thrust levels

significantly above the cold-gas contribution alone, identifying distinct discharge modes, and outlining the design and operational changes required to approach the targeted performance.

Keywords: Pulsed thruster, Magnetoplasmadynamics, Thrust determination

1 Introduction

Pulsed, gas-fed electric propulsion systems are a promising option for future small satellite missions, combining high specific impulse with scalability and flexible operation. For their qualification and integration into flight missions, a reliable performance characterization with accurate impulse bit determination is required. Conventional thrust balance measurements, where the thruster is mounted directly on the pendulum, are not suitable for gas-fed concepts, as the required propellant feed lines introduce parasitic forces and couple the balance mechanically to the vacuum chamber.
In this work, an indirect thrust measurement methodology is presented and applied to the initial characterization of a prototype of the pulsed magnetoplasmadynamic thruster of the Modular Pulsed Propulsion System (MP^2S MPDT). The thruster plume is directed onto a graphite target mounted on a high-precision thrust balance, eliminating mechanical interference from the gas supply system. The impulse transfer between the argon plume and the graphite target is quantified using LAMMPS molecular dynamics simulations to obtain an impulse transfer correction factor. The resulting pendulum motion is recorded by a nanometer-resolution optical displacement sensor and processed using sinusoidal curve fitting and wavelet filtering to reduce noise while preserving the signal characteristics. A rigorous error analysis based on Gaussian error propagation incorporates uncertainties from calibration, respective sensor resolutions and errors, geometry, timing, frequency determination, damping and impulse transfer. The methodology is used to determine impulse bit, specific impulse and thrust efficiency of the MP^2S MPDT, and the results are discussed.

2 Test Setup

The test setup for measuring the thrust, impulse bit, specific impulse and thrust efficiency of gas-fed pulsed thrusters consists of a vacuum tank and a thrust balance assembly.

2.1 Vacuum Facility

The thrust balance and thruster are housed in vacuum chamber 16, shown in Figure 1, which is the largest vacuum chamber in the IRS PPT lab. It has a diameter of 0.5 m and a length of 1.6 m. The chamber is evacuated using a Pfeiffer Duo 016B pump as a first stage and a Pfeiffer TPU 170 turbopump as a second stage to achieve a vacuum pressure of 1×10^{-3} Pa.[1]

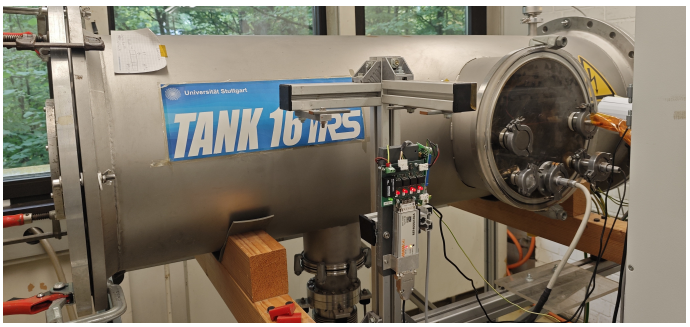


Fig. 1: Vacuum chamber 16

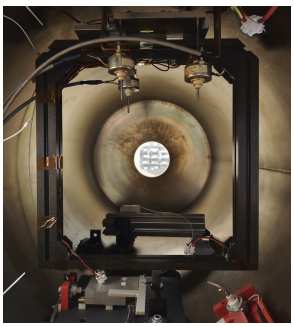


Fig. 2: Thrust balance pendulum

2.2 Thrust Balance

The impulse bit is measured using the IRS thrust balance developed by Montag, shown in Figure 2.[2] The setup consists of a pendulum supported by four pivot bearings, an optical displacement sensor with a resolution of 5 nm which is used to record pendulum oscillation, and an electrostatic comb for calibration.
The four type E-10 pivot bearings by GAD Elektronikkomponenten have a combined spring constant of $9.58\,\mathrm{N\,cm\,rad^{-1}}$ and can be used as electrical feedthroughs that do not introduce added friction, which is necessary for calibration. Pendulum and sensor alignment is achieved using five Nanotec® LP3575S0504-TR3.5X1 linear actuators. Because the MP^{2}S MPDT is gas-fed, an indirect measurement technique is used in which the thruster is not mounted on the pendulum (see Subsection 2.3).

2.3 Indirect Measurement Technique

Typical thrust balance measurements where the thruster is mounted on the pendulum are not feasible for gas-fed thrusters, since the gas supply lines interfere with the very low friction operation of the pendulum. Multiple methods were examined to solve this problem.

1. Gas tank as part of the thruster assembly on the pendulum.
2. Small external gas tank mounted on the pendulum.
3. Thruster fires upon a graphite target which imparts the plume impulse onto the pendulum.

All these methods come with new problems:

1. Infeasible for early prototypes. Additionally, failure of the tank would lead to catastrophic failure of the turbopump.
2. Failure of the tank would lead to catastrophic failure of the turbopump.
3. Added uncertainty due to unknown impulse transfer from the plume to the graphite target.

Since methods 1 and 2 introduce unacceptable safety risks, method 3 is chosen. The impulse transfer between the argon plume of the MP^{2}S MPDT and the graphite target

is gauged using LAMMPS simulations.[3] More information on these simulations is found in Section 3.

Figure 3 shows a schematic of the measurement setup. The numbered components

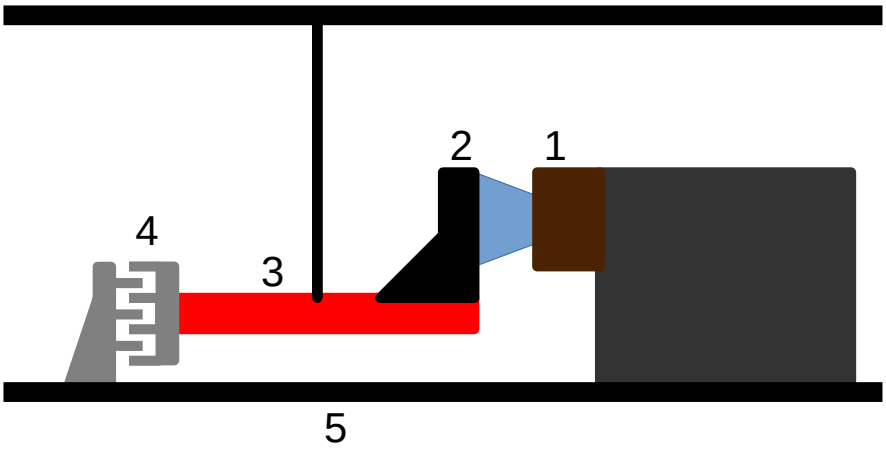


Fig. 3: Schematic of the indirect measurement setup

are:

1. Thruster.
2. Graphite target.
3. Thrust balance pendulum.
4. Electrostatic calibration comb.
5. Vacuum chamber wall.

2.4 Additional Diagnostics

In addition to the pendulum oscillation measurements, the pressure inside the thruster plenum is monitored using a TEI PST867 pressure sensor mounted in the plenum manifold. The capacitor discharge during thruster operation is recorded with a Testec TT-SI 9010 high-voltage differential probe and a LeCroy Wavesurfer 424 oscilloscope. A schematic of the electrical setup for charging the capacitor bank and recording the discharge is shown in Figure 4.

3 Impulse Transfer Simulations

To accurately measure the performance data of the MP^{2}S MPDT, it is necessary to know how much of the argon's impulse is transferred to the graphite target. Molecular dynamics simulations are used to find the impulse transfer efficiency.

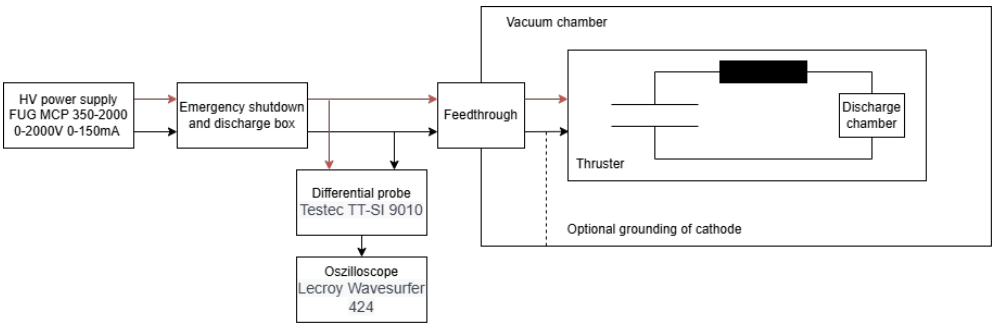


Fig. 4: Capacitor bank charging and discharge recording setup

3.1 Impulse Transfer

When a very light body, such as an argon atom, collides with a much heavier solid body in an ideal, one-dimensional elastic collision, the light body is, in the limit of an infinite mass ratio, reflected with approximately unchanged speed but reversed direction. In this limit, the heavy body consequently receives an impulse that approaches twice the light body's initial impulse.
In real materials, part of the kinetic energy is converted into internal energy of the heavy body via lattice vibrations, phonons and plastic deformation, so that impulse transfer is accompanied by heating and possibly surface modification. For a macroscopic target bombarded by many light particles, the net impulse on the target is then determined by the ensemble of microscopic collisions, including scattering angles, energy loss mechanisms and surface properties, rather than by a single two-body collision.

3.2 LAMMPS Molecular Simulation

LAMMPS (Large-scale Atomic/Molecular Massively Parallel Simulator) is an open-source molecular dynamics code designed for simulations of atomic, molecular and mesoscale systems. It supports a wide range of interaction potentials (e.g. Lennard-Jones, EAM, Tersoff, ReaxFF, AIREBO), boundary conditions and ensembles, making it suitable for modelling solid materials, fluids, plasmas and their interfaces. For plume–surface interaction problems, LAMMPS can be used to model the target material at the atomic level and track the trajectories, energy dissipation and momentum transfer of incident particles to derive effective impulse transfer correction factors.[3]
A visualization of the initial conditions of a scaled down example of the simulation is shown in Figure 5.

3.3 Interaction Potentials

In this paper, interactions between carbon and argon are relevant. Different interaction potentials are required to model them.
For argon-argon and argon-carbon interactions, a Lennard-Jones potential is used, which is an established standard for noble gases. Cole applies this potential to Ar-C

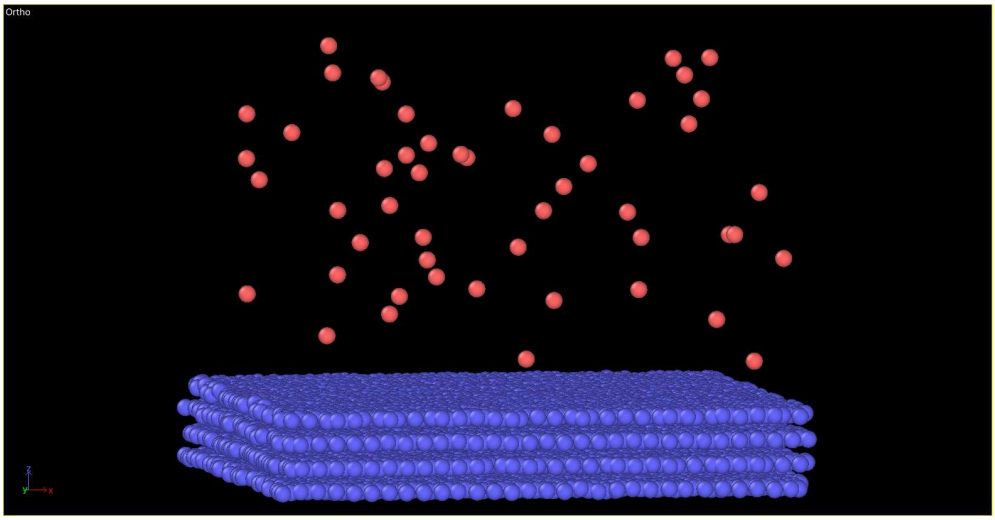


Fig. 5: Visualization of a lower scale simulation initial condition using ovito.[4] Argon in red, carbon in blue. Width of the graphite slab 8.5 nm

interactions as well and determines the relevant potential well depths and cutoff distances list in Table 1.[5]
Additionally, a Ziegler-Biersack-Littmark potential for close range interactions is implemented for argon-carbon interactions. This potential is designed for high-energy collisions and very short interatomic distances, where nuclear repulsion and electronic screening dominate.[6] Combining Ziegler-Biersack-Littmark and Lennard-Jones potentials avoids unphysical atom overlap and excessive penetration depths that would occur if the purely attractive–repulsive Lennard-Jones form were extrapolated to very small separations, which is crucial for sputtering, implantation, or impact processes.
Graphite-graphite interactions are modeled using an adaptive intermolecular reactive bond order (AIREBO) potential, which is specifically made to model covalent bonds in carbon systems. It is tuned to accurately capture structural, mechanical and thermodynamic properties of carbon allotropes such as graphite.[7]

Table 1: Coefficients for Lennard-Jones potentials

Atom types	Potential well depth	Cutoff distance
Ar-Ar	0.0122 eV	3.35 Å
Ar-C	0.0051 eV	3.1 Å

3.4 Simulation Boundary Conditions

The LAMMPS simulation is set up to represent a simplified model of the phenomenon of argon plasma being shot toward a graphite target.

3.4.1 General Boundary Conditions

The density of a real pulsed plasma thruster exhaust plume is generally in the range of $1 \times 10^{20}\,\mathrm{m}^{-3}$. Such a low density together with the requirement to simulate a numerically significant number of argon atoms would lead to a very large amount of carbon atoms for the graphite target, producing immense computational requirements. Thus, a density of $1 \times 10^{23}\,\mathrm{m}^{-3}$ is used in the simulations. Preliminary simulations with different densities show this to be sufficiently low to avoid interaction of the argon atoms.
The argon is modeled as a gas instead of a plasma, since Coulomb interactions are negligible due to the low density, and the plume is assumed quasi-neutral. 50 argon atoms are simulated.
The graphite structure is modeled using covalent bonds. The simulation domain entails four graphite layers.
All atoms vibrate at 300 K.

3.4.2 Argon Velocity

Since the exhaust velocity of the MP^{2}S MPDT is not yet known, the influence of varying argon velocities must be studied. While the final thruster is planned to achieve a specific impulse of around 3000 s, lower performance is expected from earlier prototypes. Therefore, specific impulses ranging from 250 s to 3000 s, corresponding to argon velocities between $2.453\,\mathrm{km\,s}^{-1}$ and $29.43\,\mathrm{km\,s}^{-1}$ are studied here.
Additionally, the argon velocity at cold gas conditions is of interest. A maximum for this velocity is obtained assuming isentropic expansion of the pressurized argon in the plenum. This yields

$$v_{Ar} = \sqrt{\frac{2\kappa}{\kappa - 1} R T \left[1 - \left(\frac{p_2}{p_1}\right)^{\frac{\kappa-1}{\kappa}}\right]} = 553.6\,\mathrm{m\,s}^{-1} \tag{1}$$

with $\kappa = \frac{5}{3}$, $R = 208.1\,\mathrm{J\,kg}^{-1}\,\mathrm{K}$, a standard lab temperature $T = 295.15\,\mathrm{K}$, the typical plenum pressure $p_1 = 20\,000\,\mathrm{hPa}$ and the typical vacuum pressure $p_2 = 0.4\,\mathrm{Pa}$. 39 total simulations are carried out, 3 for each of the argon velocities listed above. For now, the incident argon velocity vector is always normal to the graphite surface.

3.5 Impulse Transfer Correction Factor Determination

During the simulation, the total axial impulse of all carbon atoms in the graphite and of all argon atoms is tracked. Once all argon atoms have impacted the graphite and the momentum transfer is complete, the ratio of the graphite's final impulse to the

argon's initial impulse quantifies how much of the argon's initial impulse has been transferred to the graphite in the axial direction, which is the relevant direction for the measurement. The impulse transfer correction factor is therefore defined as

$$c_\mathrm{i} = \frac{J_\mathrm{Graphite,end}}{J_\mathrm{Argon,init}}. \tag{2}$$

3.6 Simulation Results

Impulse transfer correction factors over the specific impulse are shown in Figure 6. The plotted line is a least-squares fit of the sum of two exponential functions as described in Equation 3:

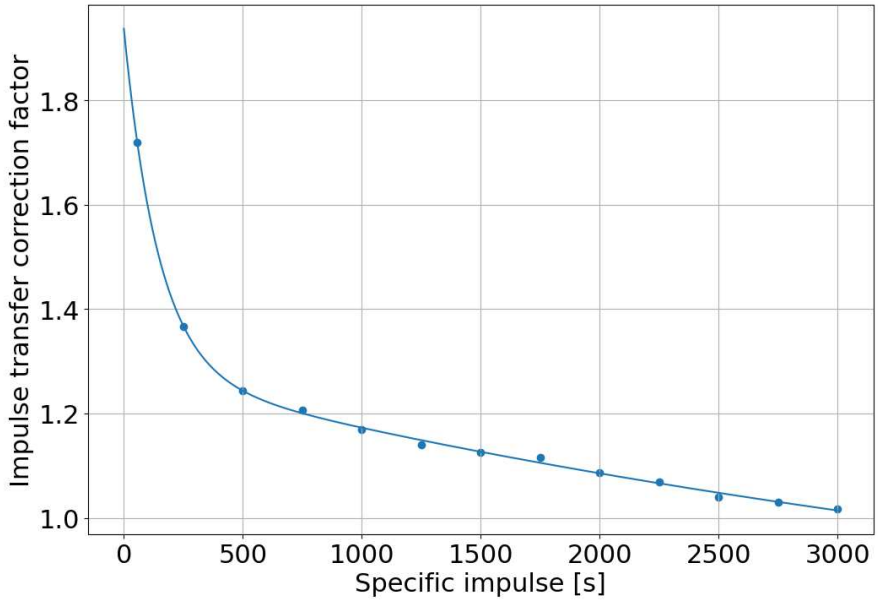


Fig. 6: Impulse transfer correction factors over specific impulse

$$c_\mathrm{i} = a \cdot e^{-b \cdot I_\mathrm{sp}} + c \cdot e^{-d \cdot I_\mathrm{sp}} + e \tag{3}$$

with the coefficients listed in Table 2.

The coefficient of determination is $R^2 = 0.9992$, implying an excellent fit.

Table 2: Coefficients of Equation 3

a	b	c	d	e
0.659 758 059	$6.866\,517\,12 \times 10^{-3}\,\mathrm{s}^{-1}$	0.591 864 494	$1.964\,921\,71 \times 10^{-4}\,\mathrm{s}^{-1}$	0.685 765 751

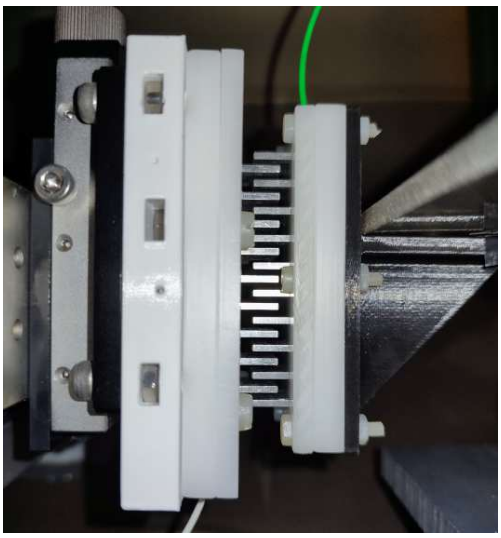


Fig. 7: Electrostatic calibration comb

4 Signal Preprocessing

The oscillation signal captured by the optical sensor of the thrust balance is noisy, decreasing the measurement accuracy. A rigorous denoising strategy is employed. Suitable denoising algorithms are found via capturing the baseline noise when the pendulum is fastened, and tested on 59 oscillation measurements. For the oscillation before thruster ignition, a sinusoidal curve fit is chosen for noise reduction, while a wavelet filter is applied post-ignition. Both methods reduce the RMS noise amplitude by 40% while keeping the signal intact as shown by the normally distributed residuals

$$r = y - \hat{y} \tag{4}$$

with the raw oscillation data y and the processed data $\hat{y}$. More information on the noise reduction is provided by Fritzsche. [1] Ultimately, the remaining noise with an RMS amplitude of 30 nm is handled as an error source in Section 7.

5 Calibration

Before the evaluation of the oscillation data to find the performance metrics becomes possible, the total inertia of the pendulum must be obtained using a calibration procedure. This calibration procedure is performed using an electrostatic comb setup as seen in Figure 7. The comb, of which one half is mounted to the pendulum and one half is mounted to the vacuum chamber, is used in conjunction with an electric pulse generator to impart a precisely known impulse onto the pendulum: the voltage-force

relationship is known, so the impulse bit can be integrated over the electric pulse as

$$I_{\mathrm{bit,c}} = \int_{t_{\mathrm{pulse}}} F(U)dt \tag{5}$$

where $F(V) = 8.863 \times 10^{-7}\,\mathrm{N\,V^{-2}}U^2$. This known impulse bit together with the resulting oscillation curve yields the total inertia of the pendulum according to

$$J = \frac{I_{\mathrm{bit,c}} \cdot l_{\mathrm{th,c}}}{\frac{\omega_{\mathrm{D}}\left(\frac{q_{\mathrm{c1}}}{e^{-D\omega t_{\mathrm{c1}}}} - q_{\mathrm{c0}}\cos(\omega_{\mathrm{D}} t_{\mathrm{c1}})\right)}{\sin(\omega_{\mathrm{D}} t_{\mathrm{c1}})} - D\,\omega\,q_{\mathrm{c0}} + q_{\mathrm{c-1}}\,\omega\,\sin(\omega t_{\mathrm{c-1}})}. \tag{6}$$

with Index c denoting values found in the calibration measurement. The calibration results in a pendulum inertia of $0.1133\,\mathrm{kg\,m^2}$.

6 Performance Metrics Determination

The main performance metric determined using the thrust balance pendulum is the impulse bit. The specific impulse and thrust efficiency can be calculated from there afterwards.
The impulse bit can be calculated from geometrical data on the pendulum and the oscillation curve recorded by the optical displacement sensor as

$$I_{\mathrm{bit}} = \frac{J}{c_{\mathrm{i}} l_{\mathrm{th}}}\left(\frac{q_1 - q_0\cos(\omega t_1)}{\sin(\omega t_1)}\omega - (-q_{-1}\omega\sin(\omega t_{-1}))\right). \tag{7}$$

The total pendulum inertia is J, the distance of the thrust vector from the bearing center of the pendulum is l_{th} and the impulse transfer correction factor is c_{i}. The pendulum deflection is q with index 0 at ignition time, index 1 at the first extremum after ignition and index -1 at the last extremum before ignition, the angular frequency is ω, the time at the first extremum after ignition is t_1 and the time at the last extremum before ignition is t_{-1}.[1, 2, 8] Notably, this equation does not include the damping of the pendulum. This is explained in Section 7.
From here, I_{sp} and thrust efficiency are calculated as

$$I_{\mathrm{sp}} = \frac{I_{\mathrm{bit}}}{g_0 m_{\mathrm{bit}}} \tag{8}$$

with earth's gravitational acceleration g_0 and mass bit m_{bit}, and

$$\eta_{\mathrm{T}} = \frac{I_{\mathrm{bit}}^2}{2 m_{\mathrm{bit}} E_0} \tag{9}$$

with the pulse energy

$$E_0 = \frac{1}{2}CU^2 \tag{10}$$

with the capacitance $C = 4.94 \times 10^{-4}\,\mathrm{F}$ and the capacitor bank voltage U.

6.1 Mass Bit

The thruster fluidic system consists of a fill valve, a plenum and a blow valve, as seen in Figure 8. The mass bit can be determined using the pressure difference in the

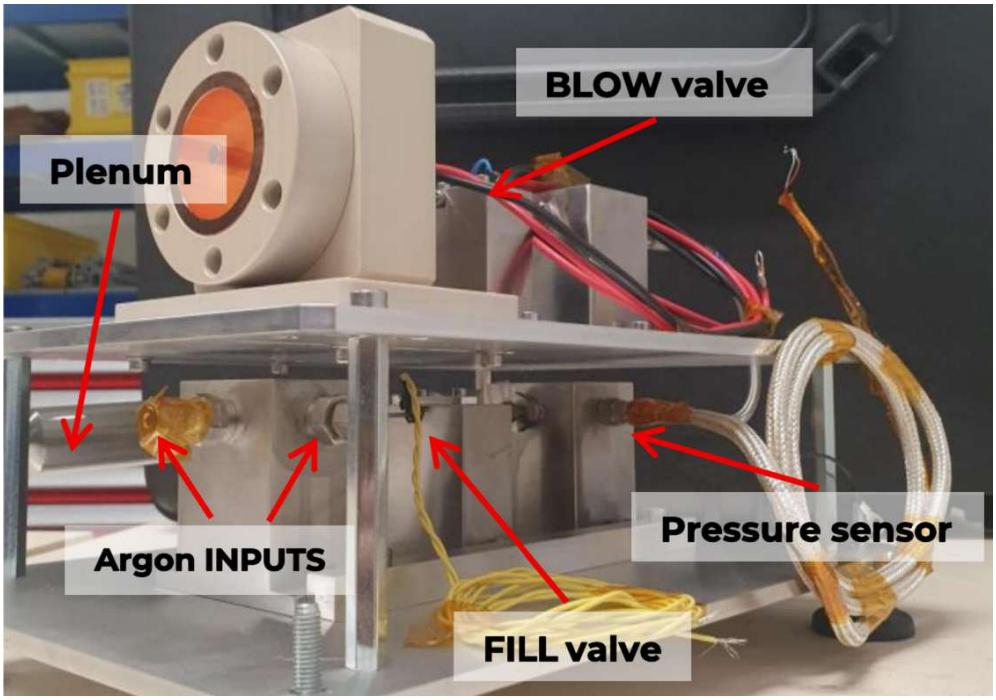


Fig. 8: Fluidic system of the MP^{2}S MPDT prototype

plenum which holds pressurized propellant. Since argon behaves like an ideal gas, the mass bit is

$$m_{\text{bit}} = \Delta m = \frac{\Delta p V}{RT} \tag{11}$$

where Δ describes the difference between values before and after the pulse, and $R = 208.1\,\text{J}\,\text{kg}^{-1}\,\text{K}^{-1}$ is the specific gas constant for argon. V is the volume of gas between the two valves and equals $58.2\,\text{cm}^3$. The lab temperature is $T = 22\,^\circ\text{C}$. It is assumed that the temperature difference pre- and post-pulse is negligible. The thermal time constant of the plenum system is

$$\tau = \frac{m_{plenum} c_{p,316\text{L}}}{\alpha A} = 9623\,\text{s} \tag{12}$$

with $m_{\text{plenum}} = 0.1581\,\text{kg}$, $c_{p,316\text{L}} = 500\,\text{J}\,\text{kg}^{-1}\,\text{K}^{-1}$ [9], the inner surface area of the plenum $A = 1.021 \times 10^{-2}\,\text{m}^2$, and the heat transfer coefficient between the wall and the argon $\alpha = \frac{\lambda}{r_{plenum}} = 0.8045\,\text{W}\,\text{m}^{-2}\,\text{K}^{-1}$ with $\lambda = 0.0177\,\text{W}\,\text{m}^{-1}\,\text{K}^{-1}$ [10] and the

inner plenum radius $r_{plenum} = 2.2\,\text{cm}$. α is calculated from the thermal conductivity of argon here, since the argon is assumed as stagnant. Since τ is orders of magnitude larger than the time interval between the pre- and post-pulse pressure readings, the assumption of constant temperature for the mass bit estimation is justified.

6.2 Impulse Transfer Correction Factor

The impulse transfer correction factor c_i affects the impulse bit and therefore the specific impulse. Conversely, changing the specific impulse changes the impulse transfer correction factor. As explained in Subsection 3.6, the the impulse transfer correction factor as a function of the specific impulse is described in Equation 3. The inverse function $I_\text{sp}(c_\text{i})$ is found numerically for each impulse transfer correction factor. The correct pair of specific impulse and impulse transfer correction factor can be obtained by iterating steps 2-4.

1. Start with measured $I_\text{sp,meas}$ with no correction factor applied and with $c_\text{i} = 1$.
2. Set $I_\text{sp} = \frac{I_\text{sp,meas}}{c_\text{i}}$.
3. Set $c_\text{i} = c_\text{i}(I_\text{sp})$ according to Equation 3.
4. Stop if $\left|\frac{I_\text{sp,meas}}{c_\text{i}} - I_\text{sp}(c_\text{i})\right| < \epsilon$

This yields a unique solution for all impulse transfer correction factors since $\frac{I_\text{sp,meas}}{c_\text{i}}$ and $I_\text{sp}(c_\text{i})$ plotted over $c_\text{i} = 0 - 2$ show only a single intersection.

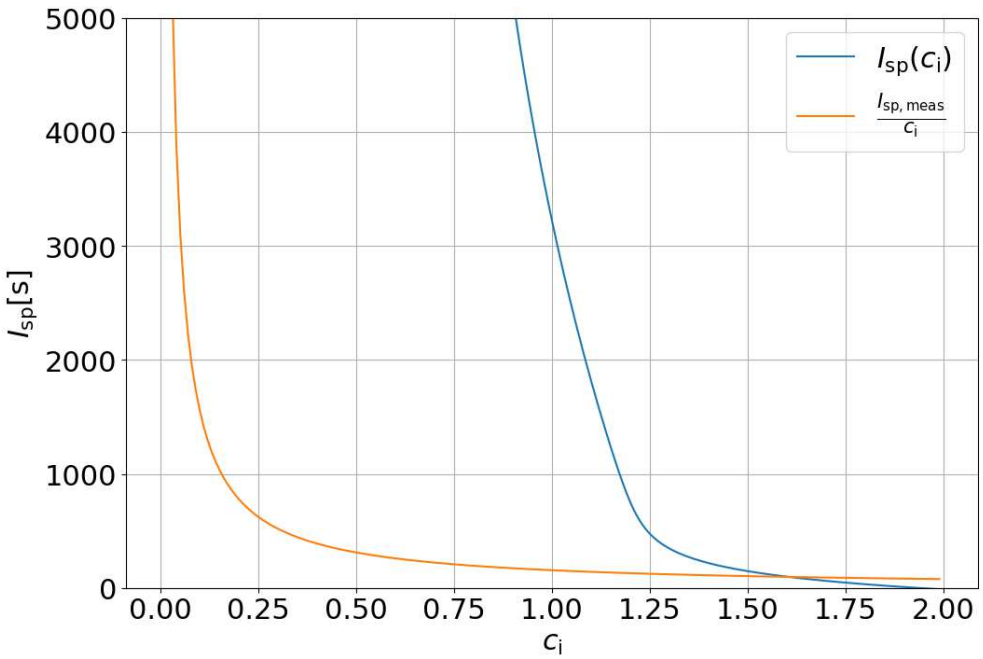


Fig. 9: $\frac{I_\text{sp,meas}}{c_\text{i}}$ and $I_\text{sp}(c_\text{i})$ plotted over $c_\text{i} = 0 - 2$ for $I_\text{sp,meas} = 155.7\,\text{s}$

7 Error Estimation

The performance parameters of the thruster prototype are subject to measurement error, which is examined here. Errors are exemplarily evaluated for an average pulse with an opening time of 350 µs and a capacitor voltage of 800 V. All error sources and their error magnitudes are listed in Table 3 alongside the typical values that are used here to obtain an exemplary error value.

Table 3: Error limits and typical values of variables used in the error estimation

Variable	**Value**	**Error**
$I_{\mathrm{bit,c}}$	$79.89\,\mu\mathrm{N\,s}$	$\pm 3.595\,\mu\mathrm{N\,s}$
D	0	$\pm 1 \times 10^{-3}$
c_{i}	1.760	± 0.1
q_{-1}	-1.016×10^{-6}	$\pm 8.253 \times 10^{-8}$
q_0	2.048×10^{-7}	$\pm 8.250 \times 10^{-8}$
q_1	-1.432×10^{-4}	$\pm 3.726 \times 10^{-7}$
$q_{\mathrm{c}-1}$	-2.048×10^{-6}	$\pm 8.250 \times 10^{-8}$
$q_{\mathrm{c}0}$	-1.389×10^{-6}	$\pm 8.251 \times 10^{-8}$
$q_{\mathrm{c}1}$	-2.799×10^{-5}	$\pm 1.225 \times 10^{-7}$
t_1	0.2920 s	± 0.005 s
t_{-1}	-0.7920 s	± 0.005 s
$t_{\mathrm{c}1}$	0.2910 s	± 0.005 s
$t_{\mathrm{c}-1}$	-0.2110 s	± 0.005 s
ω	$7.540\,\mathrm{s}^{-1}$	$\pm 0.6283\,\mathrm{s}^{-1}$
ω_{D}	$7.540\,\mathrm{s}^{-1}$	$\pm 0.6283\,\mathrm{s}^{-1}$
l_{th}	0.2770 m	± 0.001 m
l_{cth}	0.3540 m	± 0.001 m
Δp	374.1 Pa	± 52 Pa
V	$5.820 \times 10^{-5}\,\mathrm{m}^3$	$\pm 2.910 \times 10^{-6}\,\mathrm{m}^3$
T	295.15 K	± 2 K
I_{bit}	$311.0\,\mu\mathrm{N\,s}$	$\pm 26.383\,\mu\mathrm{N\,s}$
m_{bit}	0.3544 mg	$\pm 0.052\,42$ mg
C	4.940×10^{-4} F	$\pm 1.038 \times 10^{-5}$ F
U	743.1 V	± 36.01 V

7.1 Impulse Bit Error

The impulse bit measurement contains errors from multiple sources. Using Gaussian error propagation, the resulting all-sources error can be estimated according to

$$\begin{aligned}\Delta I_{\text{bit}} = \Bigg[&\left(\frac{\partial I_{\text{bit}}}{\partial I_{\text{bit,c}}}\right)^2 (\Delta I_{\text{bit,c}})^2 + \left(\frac{\partial I_{\text{bit}}}{\partial q_1}\right)^2 (\Delta q_1)^2 + \left(\frac{\partial I_{\text{bit}}}{\partial q_0}\right)^2 (\Delta q_0)^2 \\ &+ \left(\frac{\partial I_{\text{bit}}}{\partial q_{-1}}\right)^2 (\Delta q_{-1})^2 + \left(\frac{\partial I_{\text{bit}}}{\partial D}\right)^2 (\Delta D)^2 + \left(\frac{\partial I_{\text{bit}}}{\partial c_{\text{i}}}\right)^2 (\Delta c_{\text{i}})^2 \\ &+ \left(\frac{\partial I_{\text{bit}}}{\partial q_{\text{c1}}}\right)^2 (\Delta q_{\text{c1}})^2 + \left(\frac{\partial I_{\text{bit}}}{\partial q_{\text{c0}}}\right)^2 (\Delta q_{\text{c0}})^2 + \left(\frac{\partial I_{\text{bit}}}{\partial q_{\text{c}-1}}\right)^2 (\Delta q_{\text{c}-1})^2 \\ &+ \left(\frac{\partial I_{\text{bit}}}{\partial t_{-1}}\right)^2 (\Delta t_{-1})^2 + \left(\frac{\partial I_{\text{bit}}}{\partial t_1}\right)^2 (\Delta t_1)^2 + \left(\frac{\partial I_{\text{bit}}}{\partial t_{\text{c}-1}}\right)^2 (\Delta t_{\text{c}-1})^2 \\ &+ \left(\frac{\partial I_{\text{bit}}}{\partial t_{\text{c1}}}\right)^2 (\Delta t_{\text{c1}})^2 + \left(\frac{\partial I_{\text{bit}}}{\partial \omega}\right)^2 (\Delta \omega)^2 + \left(\frac{\partial I_{\text{bit}}}{\partial \omega_{\text{D}}}\right)^2 (\Delta \omega_{\text{D}})^2 \\ &+ \left(\frac{\partial I_{\text{bit}}}{\partial l_{\text{th}}}\right)^2 (\Delta l_{\text{th}})^2 + \left(\frac{\partial I_{\text{bit}}}{\partial l_{\text{cth}}}\right)^2 (\Delta l_{\text{cth}})^2 \Bigg]^{1/2}\end{aligned} \tag{13}$$

with I_{bit} as in Equation 14. This yields an absolute error of $\Delta I_{\text{bit}} = \pm 29.98\,\mu\text{N s}$ and a relative error of $\pm 8.921\%$.

7.1.1 Oscillation Measurement Error

The oscillation of the pendulum is measured by the displacement sensor with a resolution of 5 nm, leading to an uncertainty of ± 2.5 nm. Considering the remaining noise after preprocessing, which has an approximate RMS amplitude of 30 nm, the uncertainty of all oscillation values is taken as 32.5 nm. Additionally, the timing accuracy is limited by the sampling rate of 100 Hz to ± 0.005 s. The frequency errors stem from the inherent frequency resolution of a Fourier transformation of a 10 s signal. Moment arm lengths are measured to an accuracy of ± 1 mm. Additionally, the uncertainty of the calibration procedure is $\pm 4.5\%$.

7.1.2 Damping

Damping was omitted in the performance metrics determination, since the absolute measurement error of the damping is much larger than the damping itself. In the error analysis, the damping is considered according to the expanded impulse bit equation

$$I_{\text{bit}} = \frac{J}{l_{\text{th}}} \left(\frac{\frac{q_1}{e^{-D\omega t_1}} - q_0 \cos(\omega_{\text{D}} t_1)}{\sin(\omega_{\text{D}} t_1)} \omega_{\text{D}} - D\omega q_0 - (-q_{-1}\omega \sin(\omega t_{-1})) \right) \tag{14}$$

with the damping D and the damped frequency ω_{D}. Its error is $\pm 1 \times 10^{-3}$, since the damping of the pendulum is known to be $\leq 1 \times 10^{-3}$.

7.1.3 Impulse Transfer

Since validation of the impulse transfer simulations is still pending, no statements regarding systematic error can be made at this point. Additionally, simulations taking account different incident angles due to plume divergence are still pending. For now, an error of ± 0.1 is assumed.

7.2 Mass Bit Error

The mass bit has a dominant error source: The pressure sensor accuracy. The $-1000\,\mathrm{hPa}$ to $40\,000\,\mathrm{hPa}$ version of the PST867 lists $\pm 140\,\mathrm{hPa}$ as the error from non-linearity and hysteresis, and $\pm 820\,\mathrm{Pa}$ as the non-repeatability error. The non-linearity and hysteresis error is omitted since the measured data here is a small pressure difference instead of an absolute pressure. The non-repeatability error can be mitigated by averaging over multiple measurements, in this case 1000. This yields $\Delta(\Delta p) = \pm 52\,\mathrm{Pa}$ within 2σ.[11]
Other error sources for the mass bit are the volume between the valves and the lab temperature. $\Delta T = \pm 2\,\mathrm{K}$ and $\Delta V = \pm 2.91\,\mathrm{cm}^3$.
This yields an absolute error of $\Delta m_{\mathrm{bit}} = \pm 52.42\,\mu\mathrm{g}$ and a relative error of $\pm 14.79\%$ according to

$$\Delta m_{\mathrm{bit}} = \left[\left(\frac{\partial m_{\mathrm{bit}}}{\partial \Delta p} \right)^2 (\Delta(\Delta p))^2 + \left(\frac{\partial m_{\mathrm{bit}}}{\partial T} \right)^2 (\Delta T)^2 + \left(\frac{\partial m_{\mathrm{bit}}}{\partial V} \right)^2 (\Delta V)^2 \right]^{1/2}. \quad (15)$$

7.3 Specific Impulse Error

The specific impulse error stems from impulse bit and mass bit error. It is $\Delta I_{\mathrm{sp}} = \pm 16.82\,\mathrm{s}$ or $\pm 4.955\%$ according to

$$\Delta I_{\mathrm{sp}} = \left[\left(\frac{\partial I_{\mathrm{sp}}}{\partial I_{\mathrm{bit}}} \right)^2 (\Delta I_{\mathrm{bit}})^2 + \left(\frac{\partial I_{\mathrm{sp}}}{\partial m_{\mathrm{bit}}} \right)^2 (\Delta m_{\mathrm{bit}})^2 \right]^{1/2}. \quad (16)$$

7.4 Thrust Efficiency

The thrust efficiency error stems from impulse bit error, mass bit error, and capacitor energy error which is made up of capacitance and voltage errors.
The capacitance error measured with a RS pro LCR1703 multimeter is $\Delta C = 10.38\,\mu\mathrm{F}$ or $\pm 2.101\%$ and the voltage measurement error is $\Delta U = 36.01$ or $\pm 4.846\%$, which is a conservative estimate adding the errors of the TT-SI 9010 differential probe and the LeCroy WaveSurfer 424 oscilloscope. The resulting thrust efficiency error is $\Delta \eta_{\mathrm{T}} =$

3×10^{-4} or $\pm 25.08\%$ according to

$$\Delta\eta_\mathrm{T} = \left[\left(\frac{\partial \eta_\mathrm{T}}{\partial I_\mathrm{bit}} \right)^2 (\Delta I_\mathrm{bit})^2 + \left(\frac{\partial \eta_\mathrm{T}}{\partial m_\mathrm{bit}} \right)^2 (\Delta m_\mathrm{bit})^2 + \left(\frac{\partial \eta_\mathrm{T}}{\partial C} \right)^2 (\Delta C)^2 + \left(\frac{\partial \eta_\mathrm{T}}{\partial U} \right)^2 (\Delta U)^2 \right]^{1/2} . \tag{17}$$

8 Results

In an initial measurement campaign, impulse bit, mass bit, specific impulse and thrust efficiency were measured and evaluated for 180 pulses with blow valve opening times of 225 µs, 350 µs and 500 µs and capacitor bank voltages of 0 V (cold gas condition), ∼562 V, ∼657 V, ∼742 V, ∼822 V and ∼910 V. The results are presented in Figure 10. No measurements at the target opening time of 200 µs were performed at this point, since the valve opening is currently still unreliable below 225 µs. Efforts to increase reliability are ongoing.
The averages for all data points are compiled in Tables 4 to 6. The impulse bit increases approximately linearly with capacitor voltage and mass bit. The specific impulse increases with decreasing mass bit and increases with increased capacitor voltage. A clear trend for the thrust efficiency is not visible, but higher mass bits and lower voltages seem to increase efficiency. More data must be obtained and the accuracy of the thrust efficiency determination be increased to make definitive claims.

Table 4: Average impulse bit for all measured data points in µN s

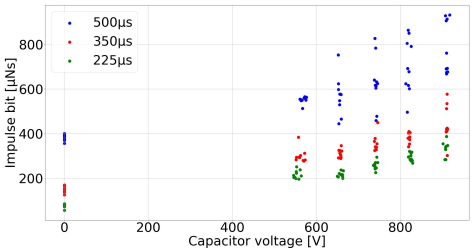
	0 V	562 V	657 V	742 V	822 V	910 V
500 µs	347.5	489.4	504.0	552.9	614.9	683.6
350 µs	142.7	276.9	286.9	317.7	348.4	398.3
225 µs	74.77	203.9	203.5	239.4	272.0	305.7

Table 5: Average specific impulse for all measured data points in s

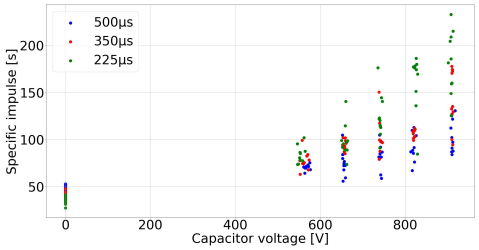
	0 V	562 V	657 V	742 V	822 V	910 V
500 µs	44.88	62.64	66.14	74.60	81.46	90.48
350 µs	39.00	71.67	86.44	93.46	96.69	127.2
225 µs	35.02	79.11	93.13	116.6	149.2	167.2

Table 6: Average thrust efficiency for all measured data points in %

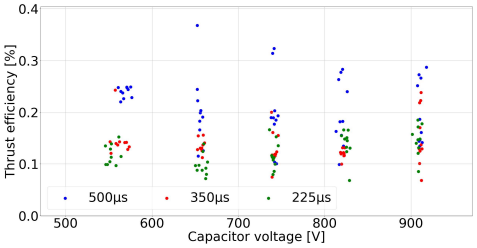
	0 V	562 V	657 V	742 V	822 V	910 V
500 µs	-	0.1881	0.1577	0.1530	0.1514	0.1509
350 µs	-	0.1253	0.1141	0.1080	0.09927	0.1185
225 µs	-	0.1049	0.08702	0.1016	0.1185	0.1232



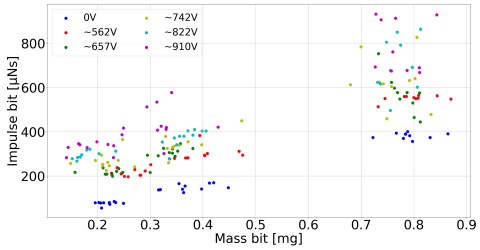
(a) Impulse bit for different blow valve opening times over capacitor voltage



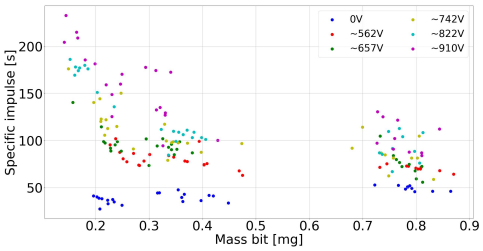
(b) Specific impulse for different blow valve opening times over capacitor voltage



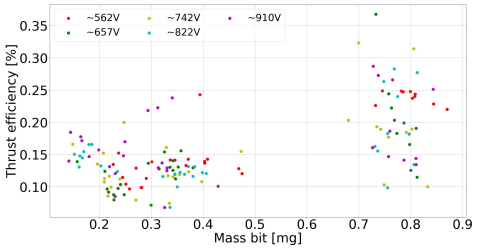
(c) Thrust efficiency for different blow valve opening times over capacitor voltage



(d) Impulse bit for different capacitor voltages over mass bit



(e) Specific impulse for different capacitor voltages over mass bit



(f) Thrust efficiency for different capacitor voltages over mass bit

Fig. 10: Results of the initial measurement campaign

8.1 Discharge Modes

The oscilloscope recordings of the capacitor discharge show at least two different modes of discharge, which are distinguished by their discharge curve as well as the resulting thruster performance. Exemplary curves can be seen in Figure 11.
Mode 2 featuring one zero pass and a negative final voltage is the dominant mode with mode 1 featuring at least two zero passes being much rarer, making up only 13 of the 150 recorded discharges. Mode 1 may comprise several modes with different numbers of zero passes and different final voltages, which will become apparent using a longer timebase for the oscilloscope recording and recording more discharge data.
The thrust efficiency of pulses where mode 1 discharge occurs is on average 77% higher than pulses where mode 2 occurs, and the specific impulse is 11% higher. This improvement arises because a smaller fraction of the input energy remains stored in the capacitor bank in mode 1, so more energy is effectively transferred to the plasma and converted into thrust.

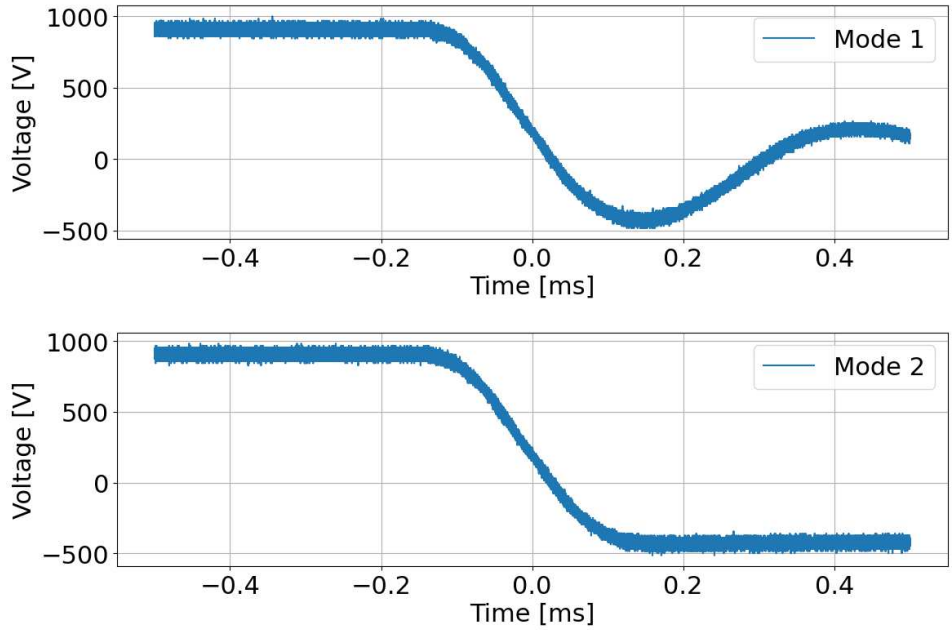


Fig. 11: Discharge modes of the capacitor bank

9 Discussion

In an initial measurement campaign, the indirect thrust measurement technique introduced in this paper and in [1] has been demonstrated to work reliably. The results show specific impulses under cold-gas conditions in the predicted range based on isentropic expansion, indicating that the measurement setup operates as intended. While

the measurement accuracy of impulse bit and specific impulse is good, and the mass bit accuracy is acceptable, the uncertainty of the thrust efficiency must be further reduced.
Although the optimal operating conditions of the MP^{2}S MPDT have yet to be determined, the results clearly indicate that the device generates thrust exceeding the cold-gas contribution alone. Under the operating conditions investigated here, the specific impulse remains far below the target value of 3000 s. This is expected, since the current device is an early prototype, and the synchronization of the valve opening and the capacitor discharge has not been optimized yet. In addition to this pending optimization, future design iterations should aim to favor discharge mode 1 (see Subsection 8.1), which is rare at the present design state, but shows both higher specific impulse and thrust efficiency.
The initial application of the impulse transfer correction yields physically consistent results: without this correction, the specific impulse under cold-gas conditions would be unrealistically high, exceeding the maximum value obtained from isentropic expansion (see Subsection 3.4.2). With the correction applied, the inferred specific impulse falls into the expected range. Nevertheless, a rigorous validation campaign for the simulation-based correction function remains an essential task for future work.

Acknowledgements. The project under which this research has been conducted has received funding from the European Union's Horizon Europe programme under grant agreement No. 101135440. The authors would like to express their sincere gratitude to the European Union for this support, which made the research presented in this paper possible. Views and opinions expressed in this paper are those of the authors only and do not necessarily reflect those of the European Union or the European Innovation Council. Neither the European Union nor the granting authority can be held responsible for them.

Declarations

Funding

The project under which this research has been conducted has received funding from the European Union's Horizon Europe programme under grant agreement No. 101135440.

Conflicts of Interest

The authors have no competing interests to declare that are relevant to the content of this article.

Data availability

The data recorded and analyzed during the current study are available from the corresponding author on reasonable request.

Code Availability

Not applicable.

Author's Contributions

Conceptualization and study design were carried out by R. Fritzsche with contributions from F. Schäfer and G. Herdrich. The test campaign was carried out by R. Fritzsche and F. Schäfer. Molecular dynamics simulations were conceptualized, planned and performed by R. Fritzsche. T. Yung, J. Scheiner, G. Brivary-Couret and L. Herrero designed and provided the device under test and contributed technical input regarding its operation and characteristics. Funding was acquired by G. Herdrich. The manuscript was written by R. Fritzsche and reviewed and edited by G. Herdrich.

References

[1] Fritzsche, R., Schäfer, F., Herdrich, G., Yordanov, V., Scheiner, J., Yung, T., Brivary–Couret, G., Herrero, L.: Thrust measurement setup for the modular pulsed propulsion system. In: 39th International Electric Propulsion Conference. https://www.electricrocket.org/IEPC_2025/London/submission_65.pdf, London (2025). IEPC-2025-065

[2] Montag, C.: Development of a flight ready pulsed plasma thruster propulsion system. PhD thesis, University of Stuttgart (2022)

[3] Thompson, A.P., Aktulga, H.M., Berger, R., Bolintineanu, D.S., Brown, W.M., Crozier, P.S., Veld, P.J., Kohlmeyer, A., Moore, S.G., Nguyen, T.D., Shan, R., Stevens, M.J., Tranchida, J., Trott, C., Plimpton, S.J.: LAMMPS - a flexible simulation tool for particle-based materials modeling at the atomic, meso, and continuum scales. Comp. Phys. Comm. **271**, 108171 (2022) https://doi.org/10.1016/j.cpc.2021.108171

[4] Stukowski, A.: Visualization and analysis of atomistic simulation data with OVITO-the Open Visualization Tool. MODELLING AND SIMULATION IN MATERIALS SCIENCE AND ENGINEERING **18**(1) (2010) https://doi.org/10.1088/0965-0393/18/1/01501

[5] Cole, M.W., Klein, J.R.: The interaction between noble gases and the basal plane surface of graphite. Surface Science **124**(2), 547–554 (1983) https://doi.org/10.1016/0039-6028(83)90808-7

[6] Ziegler, J.F., Biersack, J.P.: In: Bromley, D.A. (ed.) The Stopping and Range of Ions in Matter, pp. 93–129. Springer, Boston, MA (1985). https://doi.org/10.1007/978-1-4615-8103-1_3

[7] Stuart, S.J., Tutein, A.B., Harrison, J.A.: A reactive potential for hydrocarbons

with intermolecular interactions. The Journal of Chemical Physics **112**(14), 6472–6486 (2000) https://doi.org/10.1063/1.481208

[8] Montag, C., Schönherr, T., Herdrich, G., Amo, J.: Updates towards an automated vertical impulse pendulum and performance characterization of petrus 2.0. (2018)

[9] Materials: Stainless Steel 316L - 1.4404 Data Sheet. https://www.thyssenkrupp-materials.co.uk/stainless-steel-316l-14404.html (2025)

[10] Kleiber, M., Joh, R.: D3 Stoffwerte von sonstigen reinen Fluiden. In: VDI-Wärmeatlas. VDI-Buch., pp. 357–488. Springer, Berlin, Heidelberg (2013). https://doi.org/10.1007/978-3-642-19981-3_3 . https://doi.org/10.1007/978-3-642-19981-3_3

[11] BIPM, IEC, IFCC, ILAC, ISO, IUPAC, IUPAP, OIML: Evaluation of measurement data — Guide to the expression of uncertainty in measurement. Joint Committee for Guides in Metrology, JCGM 100:2008. https://doi.org/10.59161/JCGM100-2008E